Matter

CellPress

Article

Induced Charge Anisotropy: A Hidden Variable Affecting Ion Transport through Membranes

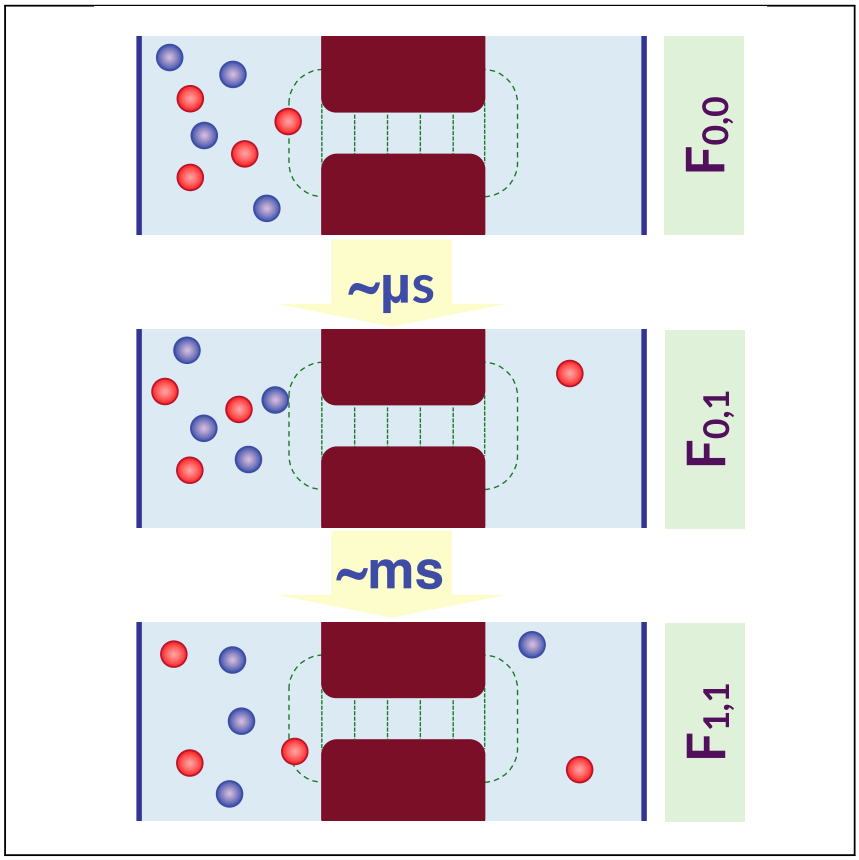

Conventional molecular simulations are generally incapable of capturing the kinetics of solute transport through ultra-selective membranes. Here, we use a recently developed path-sampling technique called jumpy forward-flux sampling to accurately and efficiently compute long passage times for sodium and chloride ions traversing a nanoporous graphitic membrane. We also demonstrate that an ion's passage is not only impeded by its partial dehydration but also by a negative restraining force due to the charge anisotropy that it induces at its rear.

Hessam Malmir, Razi Epsztein, Menachem Elimelech, Amir Haji-Akbari

amir.hajiakbaribalou@yale.edu

HIGHLIGHTS

A novel path-sampling technique is used to probe ion transport through nanopores

The method efficiently predicts long ion passage times and the transport mechanism

A traversing ion induces charge anisotropy at its rear, which pulls it backward

Ion transport is impeded due to partial dehydration and electrostatic pullback

3 **Understanding**
Dependency and conditional studies on material behavior

Malmir et al., Matter 2, 1–16
March 4, 2020
https://doi.org/10.1016/j.matt.2019.12.022

Please cite this article in press as: Malmir et al., Induced Charge Anisotropy: A Hidden Variable Affecting Ion Transport through Membranes, Matter (2019), https://doi.org/10.1016/j.matt.2019.12.022

Matter

CellPress

Article

Induced Charge Anisotropy: A Hidden Variable Affecting Ion Transport through Membranes

Hessam Malmir,[1,2] Razi Epsztein,[1,3] Menachem Elimelech,[1] and Amir Haji-Akbari[1,4,*]

SUMMARY

The ability of semipermeable membranes to selectively impede the transport of undesirable solutes is key to many applications. Yet obtaining a systematic understanding of how membrane structure affects selectivity remains elusive due to the insufficient spatiotemporal resolution of existing experimental techniques and the inaccessibility of relevant solute transport timescales to conventional molecular simulations. Here, we utilize jumpy forward-flux sampling to probe the transport of sodium and chloride ions through a graphitic membrane with sub-nanometer pores. We find chlorides to traverse the pore at rates over two orders of magnitude faster than sodiums. We also identify two major impediments to the transport of both ion types. In addition to the partial dehydration of the leading ion, its traversal induces charge anisotropy at its rear, which exerts a net restraining force on the ion. Charge anisotropy is therefore a crucial hidden variable controlling the kinetics of ion transport through nanopores.

INTRODUCTION

The ability to control ion and solute transport through membranes is central to many processes in chemistry, biology, and materials science, such as water desalination,[1,2] chemical separation of gases,[3,4] ions,[5] organic solvents,[6] and viruses,[7] and *in vivo* transport of ions, pharmaceuticals, and nutrients through biological membranes[8] and channel proteins.[9] Most such applications rely on the semipermeability of the underlying membrane, i.e., its ability to preferentially allow for the passage of some molecules and/or ions while excluding the majority of other components. Consequently, the need to improve solvent permeability and solvent-solute selectivity of membranes has been extensively addressed in recent years.[10–20] The major obstacle to enhancing selectivity is the considerable gap in our understanding of the molecular-level features that control selectivity. This is primarily due to insufficient spatiotemporal resolutions of most experimental techniques in probing the molecular mechanism of solvent and solute transport through nanopores. In principle, it is generally understood that the selectivity of a nanoporous membrane for a specific solute is mainly dictated by steric,[21] charge-exclusion,[22] and solvation[23–28] effects. More recent investigations, however, point to a more complex picture and underline the importance of other more subtle factors such as polarizability effects[29] and mechanical properties of the membrane.[30] Consequently, selectivity is affected by a complex interplay of a confluence of factors and cannot be determined by a single measure, such as ion size, charge density, or hydration energy, as demonstrated in recent experimental studies.[19] Understanding how membrane structure affects its selectivity for different types of solutes is therefore of pressing importance.

Progress and Potential

Improving solute selectivity is critical to enhancing the efficiency and sustainability of membrane separation processes. Doing so, however, requires understanding the molecular-level processes that culminate in solute transport through semipermeable membranes. Existing experimental techniques lack the spatiotemporal resolution necessary for probing such molecular-level events, and conventional simulation techniques cannot probe timescales relevant to the transport of unwanted solutes through ultra-selective membranes. Here, we use path-sampling molecular simulations to circumvent both these limitations. We not only accurately and efficiently compute arbitrarily long solute passage times but also identify induced charged anisotropy as a hidden variable affecting ion transport through nanopores. Our approach provides a scalable paradigm for computational studies of selectivity in applications such as desalination, chemical separation, and biological membrane transport.

In recent years, there has been an increased interest in using molecular simulations to study solvent and solute transport through nanoporous membranes; molecular simulations have been utilized for computing properties such as solvent permeability,[31–35] free energy barriers,[25–27,33,36,37] and solute rejection rates[31,32,34] across numerous well-defined nanoporous membranes. However, these studies either use conventional techniques, such as molecular dynamics (MD),[38] which provide unbiased kinetic and mechanistic information but cannot efficiently probe long solute passage timescales or utilize techniques such as umbrella sampling[39] that are based on applying biasing potentials along pre-specified reaction coordinates but provide no direct information about kinetics. Therefore, such traditional techniques are inadequate for comprehensively investigating the structure-selectivity relationship in ultra-selective membranes due to their limited range of accessible timescales or their inability to probe the passage kinetics altogether.

Here, we apply non-equilibrium MD simulations and jumpy forward-flux sampling (jFFS)[40] to investigate the pressure-driven transport of sodium and chloride ions across multilayer nanoporous graphitic membranes. Nanoporous graphene has been shown in numerous studies[31,33,36,41,42] to be a potential next-generation desalination membrane. Using an advanced sampling technique such as FFS, which has been successfully utilized for studying rare events, such as crystal nucleation,[43–51] hydrophobic evaporation,[52,53] and protein folding,[54] enables us to precisely and efficiently compute arbitrarily long mean passage times and to obtain a statistically representative picture of the ion transport mechanism. In the case of the hydrogen-passivated graphitic nanoporous membrane considered in this work, we find the first ion to traverse the pore to always be a chloride, with mean passage times of several microseconds. This corresponds to a solute passage ratio of one chloride per 10,000 solvent molecules. Sodium ions, however, traverse the pore over passage times close to a millisecond. This wide separation of timescales between sodium and chloride transport results in the emergence of a reversal potential across the membrane. We also demonstrate that for both ion types, the kinetics of ion transport is governed by partial dehydration and the reorganization of the hydration shell, as well as the emergence of charge anisotropy in the salty feed during the transport process. This induced charge anisotropy is a previously overlooked hidden variable that has a strong impact on the kinetics and mechanism of ion transport.

METHODS

System Description and Preparation

The model filtration system considered in this work is comprised of a three-layer graphitic membrane with a sub-nanometer cylindrical nanopore, two pistons, 5,720 water molecules, 95 sodium ions, and 95 chloride ions (Figures 1A and 1B). The details of the simulation setup are described in the Supplemental Information. At the beginning of the simulation, the container on the left is composed of ~3,400 water molecules and all the ions, corresponding to a NaCl concentration of 1.5 M, and the container on the right is filled with water molecules only. The pore diameter, 0.5 $\pm$ 0.2 nm, was chosen in accordance with earlier studies of single-layer[31,33,36,41,55] and multilayer graphene,[34] which predict considerable salt rejection for pores of comparable diameters (see Supplemental Information for a detailed discussion of the source of uncertainty in pore diameter). The carbon atoms within the pore interior are all passivated with hydrogens. This choice was guided by earlier molecular simulations of desalination,[31,56] as well as the experimental realization that passivating graphene pores with hydrogen is the simplest choice for assuring their stability.[57] Moreover, our choice to consider three layers of graphene with a

[1]Department of Chemical & Environmental Engineering, Yale University, New Haven, CT 06511, USA

[2]Present address: Intelligent Systems Division, NASA Ames Research Center, Moffett Field, CA 94035, USA

[3]Present address: Faculty of Civil and Environmental Engineering, Technion—Israel Institute of Technology, Technion City, 32000 Haifa, Israel

[4]Lead Contact

*Correspondence: amir.hajiakbaribalou@yale.edu

https://doi.org/10.1016/j.matt.2019.12.022

Please cite this article in press as: Malmir et al., Induced Charge Anisotropy: A Hidden Variable Affecting Ion Transport through Membranes, Matter (2019), https://doi.org/10.1016/j.matt.2019.12.022

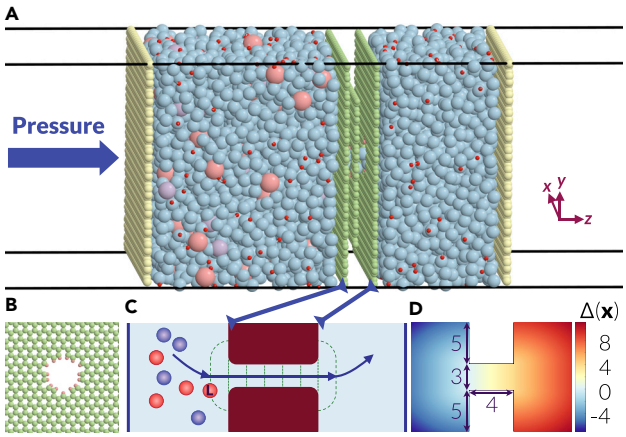

Figure 1. Overview of the Simulated System and the Utilized Order Parameter

(A and B) (A) Schematic representation of the model filtration system with the membrane (green), two pistons (yellow), water molecules (blue oxygens and red hydrogens), and sodium (light purple) and chloride (peach) ions. The cross-section of the graphitic pore is depicted from above in (B) with passivating hydrogens depicted in red. Hydrostatic pressures of 195.6 bar and −0.98 bar are applied on the left and right hand side pistons, respectively.

(C) Schematic depiction of $\Delta(\mathbf{x})$, the directed curved distance from the pore entrance, with several representative milestones. $\Delta(\mathbf{x})$ increases along the direction of the arrow. The order parameter is defined as the directed curved distance of the leading ion, labeled by L.

(D) A schematic heatmap of $\Delta(\mathbf{x})$ for a hypothetical nanoporous membrane. The dimensions do not correspond to the membrane system considered in this work.

cylindrical sub-nanometer pore is to ensure that ion passage times are too long to be captured via conventional MD. Water molecules are represented using the TIP3P force field.[58] All other atoms are represented as charged Lennard-Jones particles, with the interaction parameters and partial charges adapted from Müller-Plathe,[59] Joung and Cheatham,[60] and Beu[61] (Table S1). We use PACKMOL[62] and LAMMPS[63] to generate and equilibrate 100 independent starting configurations using the procedure outlined in the Supplemental Information. This is to ensure that our findings are not affected by the particulars of our initial setup. Prior to being used in FFS calculations, each configuration is energy minimized using the FIRE algorithm[64] and subsequently equilibrated for a minimum of 10 ns at each state point using the non-equilibrium MD scheme described below.

Molecular Dynamics Trajectories

All MD simulations are conducted using LAMMPS,[63] with equations of motion integrated using the velocity Verlet algorithm[65] and a time step of 1 fs. A Nosé-Hoover thermostat[66,67] with a time constant of 0.1 ps is applied to the water molecules and sodium and chloride ions, and the carbon and hydrogen atoms within the membrane are kept fixed during the simulation. We use the SHAKE algorithm[68] to enforce the rigidity of water molecules in the TIP3P model. All long-range electrostatic interactions are estimated using the particle-particle particle-mesh (PPPM) method,[69] with a real-space short-range cutoff of 1.0 nm. Considering the inhomogeneity of the system along the z direction and to avoid well-documented artifacts arising from applying full periodic boundaries in inhomogeneous systems, the slab PPPM method[70] is utilized in which periodic boundary conditions were only applied in the x and y directions.

In order to mimic the non-equilibrium nature of desalination (i.e., the existence of an external field, such as a hydrostatic pressure gradient), we use non-equilibrium

Please cite this article in press as: Malmir et al., Induced Charge Anisotropy: A Hidden Variable Affecting Ion Transport through Membranes, Matter (2019), https://doi.org/10.1016/j.matt.2019.12.022

MD[31,33,71] in which an extra force $f_{h,z}$ was applied to the constituent atoms of each piston as follows. At every time step, F_z, the z component of the total force exerted on the $n_p = 1{,}008$ constituent atoms of each piston is computed, and a force of $F_z/n_p + f_{h,z}$ is applied to each piston atom along the z direction. The hydrostatic pressure applied to the piston is then given by $P = n_p f_{h,z}/a_p$, where a_p is the piston's surface area. This scheme was implemented in the `fix aveforce` routine of LAMMPS, which we use in order to apply hydrostatic pressures of 195.6 and −0.98 bar on the feed and filtrate pistons, respectively. In order to maintain the rigidity of the piston, no force is exerted on their constituent atoms in the x and y directions. Also, no thermostat is applied to piston atoms, and they evolve according to the microcanonical (NVE) ensemble.

FFS Calculations

Because ion transport through a nanopore is a rare event, we probe its kinetics using FFS.[72] In general, a rare event corresponds to an infrequent transition between A and B, two (meta)stable basins within the free energy landscape of the underlying system, distinguished by an order parameter $\lambda(\mathbf{x}^N)$ that quantifies the progress of transition from $A = \{\mathbf{x}^N : \lambda(\mathbf{x}^N) < \lambda_A\}$ to $B = \{\mathbf{x}^N : \lambda(\mathbf{x}^N) \geq \lambda_B\}$. FFS estimates the rate of such a transition by recursively computing the flux of trajectories that leave A and cross a succession of N intermediate milestones, $\lambda_A < \lambda_0 < \cdots < \lambda_{N-1} < \lambda_N = \lambda_B$. Unlike most other path-sampling techniques, FFS can be utilized even when the underlying dynamics is not reversible and is therefore ideal for use with the non-equilibrium MD scheme utilized here. We denote the basins of interest based on the number of each solute type in the filtrate. More precisely, $F_{p,q}$ constitutes all the configurations in which p sodiums and q chlorides are present in the filtrate. The order parameter, $\lambda(\mathbf{x}^N)$, is then constructed based on $\Delta(\mathbf{x}_i)$, the directed curved distance of solute i from the pore entrance. The isosurfaces of $\Delta(\mathbf{x}_i)$ are schematically depicted in Figure 1C, and its precise mathematical definition is given in the Supplemental Information. Intuitively, $\Delta(\mathbf{x})$ is the minimum distance that it takes for an ion at $\mathbf{x}$ to travel to reach the pore entrance. For a transition from $F_{p,q}$ to $F_{p,q+1}$, for instance, $\lambda(\mathbf{x}^N)$ is the $(q+1)$th largest $\Delta(\mathbf{x}_i)$ for all chlorides in the system. We utilize jumpy FFS (jFFS),[40] a generalized variant of FFS that we recently developed for order parameters that can undergo considerable changes between successive samplings, and the temporal coarse-graining approach described by Haji-Akbari and Debenedetti[48] with a sampling time of 0.5 ps (or 500 time steps) (see Supplemental Information for a detailed technical explanation of why jFFS needs to be used even though the order parameter used is mathematically continuous). For chlorides, we compute the mean passage times at five different temperatures, equally spaced between 280 K and 360 K; for sodium, only one calculation at 280 K is conducted. Further details about the order parameter and the algorithm are included in the Supplemental Information, and the FFS milestones are given in Table S2.

RESULTS

Water Permeability

The passage of water molecules through semipermeable membranes is not a rare event, and its kinetics can be studied using conventional MD. We analyze the MD trajectories conducted within the starting basin as part of jFFS (see Supplemental Information for details) and computed $\Delta n_{w,p}^T = n_{w,p}(t+T) - n_{w,p}(t)$, the change in the number of water molecules within the pure water container over a time window T = 5 ns. The mean passage time is then computed as $\tau_w = T/\langle \Delta n_w, p^T \rangle$. Note that individual values of $\Delta n_{w,p}^T$ computed for non-overlapping windows exhibit considerable variability, as can be seen in Figure 2A. Therefore, obtaining an accurate estimate of $\langle \Delta n_{w,p}^T \rangle$ requires analyzing trajectories initiated from a large number of independent starting

Please cite this article in press as: Malmir et al., Induced Charge Anisotropy: A Hidden Variable Affecting Ion Transport through Membranes, Matter (2019), https://doi.org/10.1016/j.matt.2019.12.022

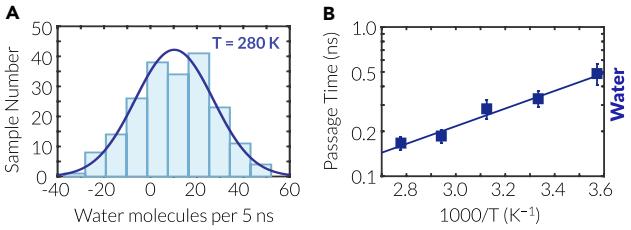

Figure 2. Kinetics of Water Transport

(A) Statistical distribution of the number of water molecules entering the pure water container during 200 non-overlapping 5-ns windows at 280 K. The dark blue curve is a Gaussian fit to the data.
(B) Arrhenius-like dependence of mean passage times for water molecules on temperature.

configurations (100 in this work). The computed τ_w values exhibit an Arrhenius dependence on temperature with an activation energy of $\Delta E_w = 11.3 \pm 3.4$ kJ/mol, which is considerably smaller than what has been reported experimentally for real semipermeable membranes with similar pore sizes, which span a wide range[9,73–75] but are generally larger than ~14.2 kJ/mol.[9] This discrepancy can be attributed to the fact that in comparison to real water, transport properties depend more weakly on temperature in the TIP3P[58] force field. For instance, for shear viscosity, which is the most relevant transport property for pressure-driven flow through a nanopore, $\Delta E_{visc}^{TIP3P} = 7.4 \pm 2.3$ kJ/mol (computed from the data in Venable et al.[76]) is almost twice smaller than the experimental value of $\Delta E_{visc}^{exp} = 15.7 \pm 0.5$ kJ/mol (computed from the data given in Kestin et al.[77]). It has indeed been argued that the activation energy for membrane permeability is bounded from below by that of transport properties of the solvent, such as shear viscosity.[78] Our computed $\Delta E_w = 11.3 \pm 3.4$ kJ/mol is indeed slightly larger than, but statistically indistinguishable from, $\Delta E_{visc}^{TIP3P} = 7.4 \pm 2.3$ kJ/mol and is consistent with other computational estimates of permeability activation energies when the TIP3P force field is utilized.[35]

The computed τ_w values can also be used for assessing the validity of the Hagen-Poiseuille law,[79] which predicts the pressure gradient needed to maintain a particular τ_w:

$$\Delta P = \frac{8\mu_w l M_w}{\pi \rho_w N_A \tau_w r^4}. \qquad \text{(Equation 1)}$$

Here, l and r are the length and the radius of the nanopore; M_w, μ_w, and ρ_w denote the molar mass, viscosity, and density of liquid water, and N_A is the Avogadro constant. We utilized the viscosity and density estimates of Venable[76] and Molinero and Moore.[76,80] respectively, and used a value of $l = 0.67$ nm based on an inter-layer distance of 0.355 nm in graphite. However, there is some uncertainty in determining r, because water molecules and the nanopore interior have comparable sizes. Depending on how the accessible volume within the nanopore is defined, r values as small as 0.15 nm (Figure S1B) and as large as 0.35 nm (Figure S1A) can be obtained (see Supplemental Information for discussions). Considering the quartic dependence of ΔP on r, this ambiguity results in ΔP values that differ by a factor of 30. At 280 K, for instance, the estimated ΔP values range between 28 bar (for $r = 0.35$ nm) and 830 bar (for $r = 0.15$ nm). Despite these uncertainties, our applied pressure gradient of ~196 bar falls within this range, which suggests that the Hagen-Poiseuille law provides reasonable estimates of solvent flux even for a sub-nanometer nanopore such as the one considered here. This is also consistent with the fact that the activation energies for permeability and viscosity are statistically indistinguishable. However, assessing the validity of the Hagen-Poiseuille law in

Please cite this article in press as: Malmir et al., Induced Charge Anisotropy: A Hidden Variable Affecting Ion Transport through Membranes, Matter (2019), https://doi.org/10.1016/j.matt.2019.12.022

Table 1. Mean First Passage Times for Water Molecules (τ_w) and Chloride Ions (τ_s), Solute Passage Ratios (S), and Total Durations of MD Trajectories during jFFS (T_{jFFS}) as a Function of Temperature

T (K)	τ_w (ns)	τ_s (μs)	S ($\times 10^{-4}$)	T_{jFFS} (μs)
280	0.487 ± 0.080	5.63 ± 0.34	0.87 ± 0.15	15.00
300	0.331 ± 0.041	2.64 ± 0.16	1.25 ± 0.17	9.42
320	0.283 ± 0.043	1.78 ± 0.11	1.59 ± 0.28	6.96
340	0.186 ± 0.018	1.33 ± 0.08	1.40 ± 0.16	5.35
360	0.167 ± 0.016	0.90 ± 0.05	1.84 ± 0.21	4.74

nanopores is a complicated proposition due to uncertainties in determining geometric properties, such as pore radius, possible breakdown of continuum assumptions at the nanoscale, such as the violation of the no-slip boundary condition and lack of a fully developed flow within the pore. Despite these uncertainties, our calculations reveal that such deviations do not have an adverse impact on the ability of the Hagen-Poiseuille flow to estimate the order of the magnitude of the solvent flux, as has been shown in earlier computational studies of liquid flow through nanopores.[81] More precisely, we do not observe a substantial enhancement in flux as has been previously reported in experimental[10] and computational[82] studies of water flow through carbon nanotubes. This is not surprising because molecular simulations have revealed that functionalized graphene surfaces possess substantially smaller slip lengths.[83,84] Indeed, the passivating hydrogens inside the pore can attract oxygen atoms in water, an effect that has also been shown to increase friction and decrease the flow rate in other systems.[85]

Kinetics of Ion Transport and Selectivity

Unlike solvent molecules, which can readily traverse the pore over sub-nanosecond timescales, the kinetics of solute transport through nanopores is usually too slow to be accurately and efficiently captured using conventional MD. Indeed, throughout our MD simulations within $F_{0,0}$ (with a total duration of ~1 μs at each temperature), we only observe one ion passage event at 360 K, and not at any other temperature. This is consistent with earlier computational studies[31–34] of nanopores with comparable sizes, all reporting 100% salt rejection for situations under which τ_s, the mean solute passage time, exceeds the duration of the conducted MD simulations. We overcome this limitation by utilizing jFFS, which enables us to accurately and efficiently estimate arbitrarily long τ_s values. In order to automatically select for the fastest passing ion, we choose our target basin as $F_{0,1} \cup F_{1,0}$ and define our order parameter as $\lambda(\mathbf{x}^N) = \max_{1 \le i \le n_s} \Delta(\mathbf{x}_i)$, where n_s is the total number of ions in the system. Since $\lambda(\mathbf{x}^N)$ does not distinguish between different ion types, it is suitable for exploring the $F_{0,0} \rightarrow F_{0,1} \cup F_{1,0}$ transition. Table 1 summarizes the computed solute passage times, which are on the order of microseconds. Estimating these microsecond-scale τ_s values with the reported level of statistical precision is still possible using conventional MD but requires tens of long MD trajectories with a total duration of several hundred microseconds. With jFFS, this is achieved with considerably shorter trajectories, and thus at a fraction of the computational cost of conventional MD. Indeed, T_{jFFS}, the total duration of MD trajectories conducted within the $F_{0,0}$ basin and between FFS milestones, is never longer than five times the mean passage time. As we discuss later, using conventional MD becomes completely impractical for passage times that are considerably longer, whereas our approach can directly estimate those with T_{jFFS} values considerably smaller than τ_s.

Please cite this article in press as: Malmir et al., Induced Charge Anisotropy: A Hidden Variable Affecting Ion Transport through Membranes, Matter (2019), https://doi.org/10.1016/j.matt.2019.12.022

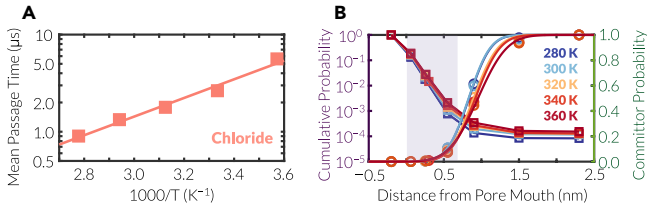

Figure 3. Kinetics of Chloride Transport

(A) Arrhenius-like dependence of mean passage time for chloride ions on temperature.

(B) Cumulative transition probabilities (squares) and committor probabilities (circles) as a function of the order parameter at different temperatures. The shaded purple region corresponds to the pore interior.

An important quantity of interest in desalination is the solute passage ratio S, defined as $S := \tau_w/\tau_s$. S corresponds to the number of solute ions/molecules that pass the pore per every traversing water molecule and depends on operating conditions such as temperature, pressure, and the concentration difference between the two containers. Table 1 summarizes the computed solute passage ratios, which are on the order of 10^{-4} (or one ion per 10,000 water molecules) and correspond to a ~99.99% salt rejection. These minuscule passage ratios are the smallest non-zero values reported in the computational literature and could not have been computed without jFFS. Yet, the ability to compute them accurately is critical to computer-aided rational design of ultra-selective membranes.

Similar to τ_w, τ_s exhibits an Arrhenius dependence on temperature (Figure 3A), with an activation energy of $\Delta E_s = 18.4 \pm 4.4$ kJ/mol. As discussed later, this barrier corresponds entirely to the transport of chloride ions. Note that ΔE_s is larger than ΔE_w, which implies the existence of additional hindrance to the passage of solutes. We describe the physical origins of such extra hindrance in our discussion of the molecular mechanism of solute transport.

Ion Transport Mechanism

In addition to probing the kinetics of ion transport, jFFS can provide detailed mechanistic information about the ion passage process. First, we observe that the leading ion to successfully traverse the pore was always a chloride. This can be attributed to favorable interactions between the positively charged passivating hydrogens in the pore interior and the chloride ions, which decrease the free energy barrier to their crossing in comparison with the positively charged sodiums that are repelled by the hydrogens. The preferential transport of negatively charged ions through hydrogenated pores is not new and has been observed previously.[41]

In order to identify the physical processes that culminate in the successful passage of a chloride ion, we first focus on the cumulative transition probability as a function of the order parameter, which is an indirect measure of how free energy changes with λ (see Equation S9 for the definition of the cumulative probability). As expected, the largest drop in cumulative probability occurs within the shaded purple region, which corresponds to the pore interior (Figure 3B). Intriguingly however, the drop in probability continues even after the ion has fully entered the pore. This can be seen more vividly in the committor probability curves of Figure 3B, which reveal the transition state (i.e., the collection of configurations with equal probability of proceeding toward either basin) to lie at around λ = 0.9 nm, i.e., right after the pore exit (see Equation S10 for the definition of committor probability, and Figure S2 for a comprehensive committor analysis, which confirms that the utilized order parameter is a

Please cite this article in press as: Malmir et al., Induced Charge Anisotropy: A Hidden Variable Affecting Ion Transport through Membranes, Matter (2019), https://doi.org/10.1016/j.matt.2019.12.022

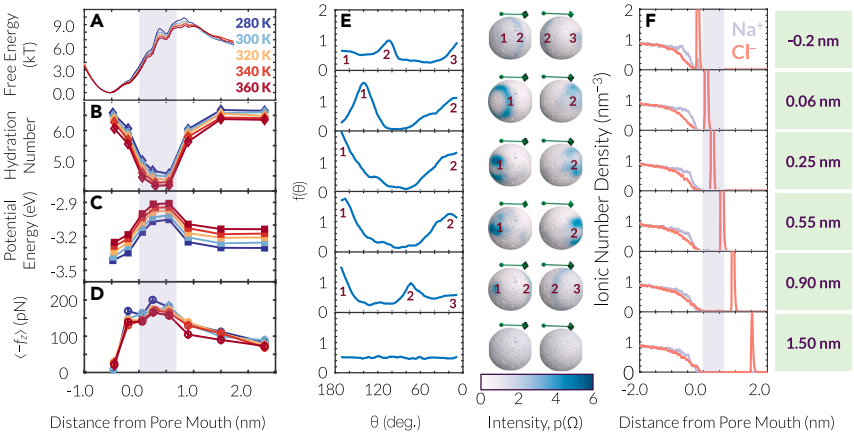

Figure 4. Mechanism of Chloride Transport through the Nanopore

(A) Free energy profiles computed from the FFS-MFPT method.

(B–D) (B) Average hydration number, (C) potential energy, and (D) restraining force in the z direction as a function of the distance from the pore mouth for the leading chloride ion at different temperatures.

(E) The orientational distribution of water molecules within the hydration shell of the leading chloride at 280 K. Here, θ is the polar angle around the z axis, which is represented by the green arrows. The numbers correspond to the peaks denoted on the full spherical orientational distribution functions. In each panel, the spheres on the right and the left are shown from the back side and front side, respectively.

(F) Number density of sodium (light purple) and chloride (dark orange) ions as a function of the curved distance from the pore mouth for different values of the order parameter. The charge anisotropy emerging close to the pore mouth results in the average restraining force along the $-z$ direction shown in (D). The order parameters on the right apply to both (E) and (F).

good reaction coordinate). This implies that the free energy profile, $F(\lambda)$, is neither flat within the pore interior nor symmetric around its central dividing plane, and instead has a maximum at $\lambda = 0.9$ nm. This is in contrast to several earlier computational studies,[23,24,26] which report $F(\lambda)$ profiles that are both flat and symmetric. The discrepancy originates from, among other things, the presence of a hydrostatic pressure gradient, which breaks the reflection symmetry of the system. The potential of mean force (PMF) calculations in all these earlier works, however, were conducted in the absence of such external driving forces.

In order to quantitatively confirm this asymmetry, we compute the free energy profiles by analyzing jFFS trajectories using the forward-flux sampling/mean first passage time (FFS-MFPT) method.[86] Even though this algorithm has been developed primarily for non-jumpy order parameters, its usage alongside jFFS is not expected to result in considerable errors because the order parameter utilized here is only slightly jumpy (Figure S3). As a consistency check, we compute $F(\lambda)$ by analyzing long unbiased MD trajectories in the $F_{0,0}$ basin and found no systematic difference between the FFS-MFPT and MD estimates. Figure 4A depicts the free energy profiles, which have two maxima at all temperatures and are asymmetric around the central dividing plane of the nanopore. The smaller maxima reside midway through the pore, and the larger maxima coincide with the transition states determined from committor probabilities (Figure 3B). The computed barriers exhibit a weak dependence on temperature, but their average of $\Delta E_{s,MFPT} = 21.7 \pm 1.1$ kJ/mol is statistically indistinguishable from the barrier estimated from the Arrhenius plot of Figure 3A, i.e., $\Delta E_s = 18.4 \pm 4.4$ kJ/mol. This further confirms the reasonable accuracy of the FFS-MFPT approach.

Please cite this article in press as: Malmir et al., Induced Charge Anisotropy: A Hidden Variable Affecting Ion Transport through Membranes, Matter (2019), https://doi.org/10.1016/j.matt.2019.12.022

In order to understand the origins of this asymmetry, we first examine the hydration properties of the leading chloride (i.e., the first chloride that has entered the pore). Figure 4B depicts its average hydration number, i.e., the average number of water molecules within a distance r_c = 0.375 nm from it. Here, r_c is the locus of the first valley of the chloride-oxygen radial distribution function depicted in Figure S4. As expected, the hydration number decreases from ~6 at $\lambda = -0.2$ nm to ~4.5 at λ = 0.55 nm, which coincides with a drop in cumulative probability. Due to the partial dehydration of the leading chloride during this initial stage, its potential energy increases and reaches a maximum at λ = 0.55 nm (Figure 4C). This increase in potential energy is also accompanied by a decrease in entropy due to structuring of the remaining water molecules within the hydration shell, as can be seen in $p(\Omega)$, the orientational distribution function for water molecules within the hydration shell (Figure 4E). Here, Ω is the solid angle and $\int p(\Omega) d\Omega = 4\pi$ (see Supplemental Information for details). The structuring begins even before the ion enters the pore, i.e., at $\lambda = -0.2$ nm, where the hydration shell comprises a front peak at θ = 0° and a rear ring at the tetrahedral angle of θ = 108°. At λ = 0.06 nm, i.e., when the ion has just entered the pore, the hydration shell preserves this qualitative structure. Only the peaks become stronger and the ring is pushed back to θ = 150°. As the ion proceeds through the pore, structuring becomes even more pronounced, and both the front peak and the rear ring turn into pairs of peaks at θ = 0° and 180°, respectively. Therefore, even though the hydration number does not change a lot within the pore interior, the hydration shell undergoes considerable reorganization. The first—and smaller—maxima of the free energy profiles of Figure 4A reside within this high-energy partially hydrated state and are almost midway through the pore.

As the ion leaves the pore, it gets rehydrated, its $p(\Omega)$ becomes more uniform, and its potential energy decreases. Nonetheless, its committor probability does not exceed 50% until λ = 0.9 nm, i.e., when the hydration number is already around six. The observed asymmetry in committor probability (Figure 3A) cannot therefore be attributed to the leading ion's partial dehydration only, because all measures of hydration are symmetric around the central dividing plane, as can be seen in Figures 4B, 4C, and 4E. This finding is in contrast to the traditional picture that partial dehydration is the primary rate-limiting step in ion transport through semipermeable membranes.[27] In order to identify alternative physical processes that cause such asymmetry, we computed $\langle \mathbf{f}(\lambda) \rangle$, the average net force exerted on the leading ion as a function of λ. Unlike $\langle f_x \rangle$ and $\langle f_y \rangle$, which are statistically indistinguishable from zero (Figure S5), $\langle f_z \rangle$ is always negative, irrespective of temperature (Figure 4D). Interestingly, a net negative force of ~100 pN is exerted on the leading ion long after it has left the pore. This restraining force competes with partial rehydration at the pore exit and is only overcome when the leading ion is fully rehydrated.

In order to identify the origin of this non-vanishing force, we probe the spatial distribution of sodiums and chlorides in the system while the leading chloride is traversing the pore. As can be seen in Figure 4F, individual ions are not uniformly distributed within the feed during that process. Instead, the number density of sodium is considerably larger than that of the chloride close to the pore mouth. Indeed, a more careful inspection of ionic distribution in the feed reveals that the first and second leading sodiums in the feed are on average closer to the pore mouth than the second and third chloride, respectively (Figure S6). This charge anisotropy generates an electric field in the z direction, which pulls back the leading chloride (the advancing peak in Figure 4F) and results in the non-vanishing $\langle f_z \rangle$ values. As discussed in detail in the Supplemental Information and depicted in Figure S7, electrostatic interactions clearly contribute to this non-vanishing $\langle f_z \rangle$, while the potential role of other factors,

Please cite this article in press as: Malmir et al., Induced Charge Anisotropy: A Hidden Variable Affecting Ion Transport through Membranes, Matter (2019), https://doi.org/10.1016/j.matt.2019.12.022

such as hydrodynamic interactions cannot be fully ruled out. The anisotropy is stronger when the leading chloride is traversing the pore and weakens slightly afterward. Nonetheless, it does not fully disappear, as can be seen in Figures S6 and S8. This is despite the fact that prior to chloride transport (i.e., within the $F_{0,0}$ basin), chloride ions are more likely to be close to the pore mouth than sodiums, as can be seen in Figure S8. However, when the leading chloride approaches and enters the pore, it induces charge anisotropy at its rear. This analysis reveals that the charge anisotropy induced by the leading ion is an important—and overlooked—hidden variable that controls ion transport through nanopores and has an impact on both the corresponding free energy barriers and passage times.

Sodium Transport Kinetics and Mechanism

Since the order parameter utilized above does not distinguish between sodiums and chlorides, it automatically selects for the ion type with the smaller passage time, namely the chloride. This means that the transition $F_{0,0} \rightarrow F_{0,1} \cup F_{1,0}$ always culminates in $F_{0,1}$. In order to probe the kinetics of sodium transport, we conduct FFS calculations with a more restrictive order parameter, namely $\lambda_+ := \max_{1 \leq i \leq n_{Na}} \Delta(\mathbf{x}_i)$, or the maximum directed curved distance of sodium ions from the pore mouth. Due to its high computational cost, we conduct this latter calculation at one temperature only, i.e., at 280 K. In order to sample the $F_{0,0}$ basin, we initiate trajectories from the endpoints of our earlier basin simulations for the $F_{0,0} \rightarrow F_{0,1} \cup F_{1,0}$ transition. Fortuitously, we find the leading chloride to have already traversed the pore in a tiny fraction of first crossings of $\lambda_{+,0} = -0.25$ nm. This percentage, however, grows exponentially in subsequent iterations, from $\approx$2% at $\lambda_{+,0} = -0.25$ nm, to $\approx$ 5.7% at $\lambda_{+,1} = 0.14$ nm, and $\approx$34% at $\lambda_{+,2} = -0.01$ nm (Figure S9). This implies that sodium transport is considerably faster when a chloride has already traversed the pore. The timescale for this faster $F_{0,1} \rightarrow F_{1,1}$ transition is of more practical relevance because sodium transport is already expected to be considerably slower than chloride transport. We therefore stopped the calculation of the $F_{0,0} \rightarrow F_{1,0}$ transition rate and launched a new jFFS simulation from 150 randomly selected configurations at $F_{0,1}$. Figure 5A depicts the computed cumulative and committor probabilities versus λ_+. The mean passage time is estimated to be $\tau_n = 900 \pm 54$ μs, which is approximately 160 times longer than the passage time for chloride at the same temperature. This wide separation of timescales is consistent with the computed free energy barriers for the respective processes, i.e., $15.5 k_B T$ for sodium (Figure 5B) and $9.8 k_B T$ for chloride (Figure 4A). Moreover, it is extremely costly to compute τ_n using conventional MD; the total length of trajectories integrated during jFFS is $T_{jFFS} \approx 17$ μs, which is only 2% of the estimated τ_n. This underscores the efficiency of jFFS in estimating arbitrarily long—and computationally inaccessible—passage times.

In order to understand the mechanism of sodium transport, we analyze jFFS trajectories in a manner similar as for chloride. Certain aspects of the mechanism are shared by both ion types, such as the asymmetry of the free energy profile (Figure 5B), the increase in potential energy within the pore interior (Figure 5D), and the existence of a net restraining force (Figure 5E). There are, however, important differences between the two processes. First, the transition state lies within the pore interior, i.e., at $\lambda_+^* \approx 0.32$ nm (Figures 5A and 5B). This is due to the larger energetic and entropic penalty of returning to the pore for the positively charged sodium that has already reached the filtrate. Therefore, the restraining force outside the pore is not strong enough to play the same role as in chloride transport. Moreover, the hydration number only decreases slightly during the transport process (Figure 5C). The fact that the leading sodium remains mostly hydrated assists it in overcoming strong electrostatic repulsions in the pore interior. Yet, even though

Please cite this article in press as: Malmir et al., Induced Charge Anisotropy: A Hidden Variable Affecting Ion Transport through Membranes, Matter (2019), https://doi.org/10.1016/j.matt.2019.12.022

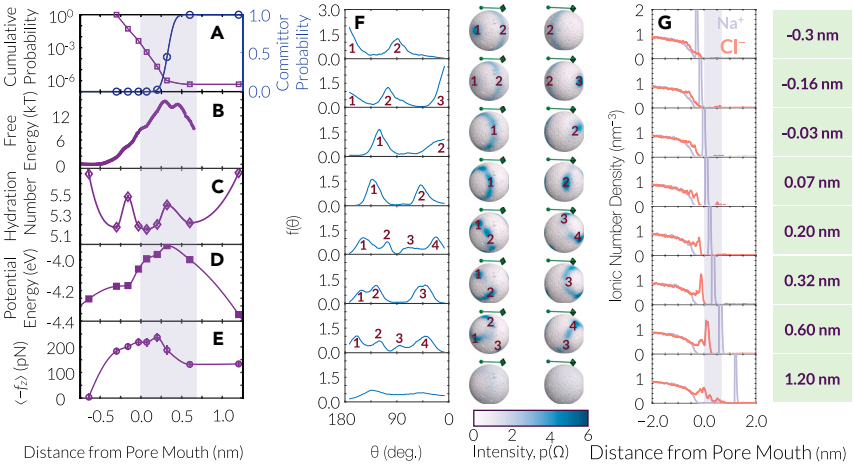

Figure 5. Kinetics and Mechanism of Sodium Transport

(A) Cumulative transition probability and committor probability as a function of the order parameter.

(B) Free energy profile computed from the FFS-MFPT method.

(C–E) (C) Average hydration number, (D) potential energy, and (E) restraining force in the *z* direction as a function of the distance from the pore mouth for the leading sodium.

(F) The orientational distribution of water molecules within the hydration shell of the leading sodium at 280 K. The numbers and colors are consistent with Figure 4E.

(G) Number density of sodium (light purple) and chloride (dark orange) ions as a function of the curved distance from the pore mouth for different values of the order parameter. The order parameters on the right apply to both (F) and (G).

the total number of hydrating waters does not change considerably, the hydration shell becomes highly organized, as can be seen in Figure 5F. The ensuing loss of entropy partly contributes to the larger free energy barrier of Figure 5B.

Another similarity between sodium and chloride transport is the emergence of charge anisotropy in the feed (Figures 4F and 5G). This effect is, however, more pronounced in the case of sodium. In particular, within a small—but considerable—number of configurations, a trailing chloride follows the leading sodium into the pore, and sometimes even all the way up to the pore exit. The presence of such a trailing chloride can facilitate the transport of the positively charged sodium. In addition, sodium transport might also catalyze the passage of that trailing chloride. This is, however, unlikely because no trailing chloride reaches the critical directed curve distance of 0.9 nm identified from Figures 3B and 4A. Similar to chloride transport, the oppositely charged trailing ions are sorted in the feed as can be seen in Figure S10. The sorting, however, is stronger than that of chloride depicted in Figure S6.

Differential Permeability and Reversal Potential

An important consequence of the differing permeabilities of different ion types is the emergence of an electrostatic potential known as reversal potential across the membrane.[87] In principle, the magnitude of the reversal potential can be computed from ionic concentrations and permeabilities using the Goldman-Hodgkin-Katz equation:[88]

$$\Delta\Psi = \frac{kT}{e}\ln\frac{p_{Na^+}[Na^+]_{feed} + p_{Cl^-}[Cl^-]_{filtrate}}{p_{Cl^-}[Cl^-]_{feed} + p_{Na^+}[Na^+]_{filtrate}},$$

where p_{Na^+} and p_{Cl^-} are sodium and chloride permeabilities, respectively, and are inversely proportional to τ_n and τ_s. Under the conditions considered here, the reversal potential is ≈ -122 mV at 280 K, which is of the same order as

experimentally reported reversal potentials for similar systems.[88] Reversal potentials are important because they are indirect measures of differing permeabilities for cations and anions. Moreover, due to the logarithmic dependence of $\Delta\Psi$ on mean passage time ratios, substantial reversal potentials only emerge when a separation of timescales exists between anion and cation transport. Our reported $\Delta\Psi$, however, is only valid for this particular feed concentration because permeabilities can in principle be affected by feed and filtrate concentrations.

DISCUSSIONS

We report the first application of an advanced path-sampling technique to study solute transport through nanoporous semipermeable membranes by utilizing jFFS and non-equilibrium MD. In particular, we probe the kinetics and microscopic mechanism of NaCl transport through a three-layer graphitic membrane with a sub-nanometer pore passivated with hydrogens. Unlike water molecules that traverse the pore over sub-nanosecond timescales, ion transport occurs over much longer timescales. The newly developed jFFS algorithm enables us to accurately and efficiently estimate mean passage times for solutes, which, in this system, were on the order of microseconds for chlorides and milliseconds for sodiums. This vast separation of timescales cannot be accurately probed using conventional techniques such as MD. Mechanistically, this separation emerges primarily due to the positive charge of the sodium ions, which are repelled by the positively charged passivating hydrogens within the pore. Therefore, even though other ionic properties, such as diffusivity and the size of the hydration shell, can affect the extent of this separation of timescales, we expect anions to always traverse the nanopores with positively charged interiors at higher rates than cations.

We also use jFFS to explore the molecular mechanism of solute transport. Due to the positive charge of passivating hydrogens within the pore interior, the first ion to pass the nanopore is always a chloride. By analyzing the configurations obtained at different jFFS milestones, we observe that both the partial dehydration of the leading chloride and charge anisotropy at the pore entrance contribute to the free energy barrier to the transport of chloride ions. This is in contrast to the traditional picture that considers partial dehydration as the main rate-limiting step for ion transport and underscores the role of induced charge anisotropy as a key hidden variable. A similar mechanism is observed for sodium transport, which involves the reorganization of its hydration shell and the emergence of charge anisotropy in the feed.

The induced charge anisotropy identified in this work is conceptually similar to the concentration polarization observed in ion exchange membranes (IEMs),[89,90] wherein the ions that are rejected by the IEM accumulate at its surface. Unlike the transient charge anisotropies observed in this work, such concentration gradients emerge under steady-state conditions and are therefore easier to characterize experimentally. Interestingly, such polarizations are also known to slow down ion transport in pressure-driven membrane processes, and our work provides a molecular-level insight into the origin of such slowdown.

The membrane system considered in this work differs from real graphitic membranes in terms of its rigidity and non-polarizability. These features have been previously shown to have an impact on solvent permeability and ion selectivity.[15,29,30,91] Consequently, properties such as mean passage times, free energy barriers, and restraining forces will change if more realistic representations are adopted. However, we do not expect our key observations, namely faster transport of anions and the emergence of charge anisotropy, to be affected by such changes. The preference

Please cite this article in press as: Malmir et al., Induced Charge Anisotropy: A Hidden Variable Affecting Ion Transport through Membranes, Matter (2019), https://doi.org/10.1016/j.matt.2019.12.022

for anions emanates from the existence of positively charged hydrogens inside the pore, and charge anisotropy arises due to partial ordering of trailing cations and anions. None of these effects is expected to disappear if the membrane is flexible. The effect of polarizability is also expected to be minimal, considering earlier calculations that have shown polarizability effects to be insignificant in monovalent salt solutions.[92,93] On a general note, simple force fields have a longstanding track record of accurately predicting the underlying physics of complex phenomena, such as the nucleation of colloidal,[46] polar,[45,48,50] or ionic[43,51] crystals, and physics of hydrophobicity[52,53] and protein folding.[94]

As discussed earlier, the difference between the passage times of sodium and chloride is expected to result in the establishment of a reversal potential across the membrane. This reversal potential should, however, not be confused with the charge anisotropy that is induced during the passage process. In other words, even if a pore does not distinguish between the ions and all ion types pass at identical rates, a similar charge anisotropy is still expected to emerge when an ion is traversing the pore.

The driven ion transport process studied in this work is non-equilibrium and irreversible in nature. It might therefore be challenging to define a proper notion of a free energy for such a driven system. The free energy profiles of Figures 4A and 5B are essentially computed based on the implicit assumption that the two containers are effectively coupled to reservoirs with constant chemical potentials. Even though this condition is not satisfied in a strict sense, the feed and filtrate concentrations do not change considerably throughout the ion transport process. The profiles obtained will therefore be reasonable estimates of the free energy landscapes of the respective ion transport processes despite being computed under such a pseudo-equilibrium condition.

The theoretical models utilized for interpreting the experimental findings of solute transport through membranes are generally based on the assumption that the process through which a solute enters a membrane and its subsequent diffusive motion within the membrane are uncorrelated. Our calculations reveal that this assumption is not always valid. In other words, when an ion enters the pore, it still needs to overcome a free energy barrier, and its motion does not follow Fickian dynamics. One cannot therefore use computational approaches that are based on the idea of decoupling, such as those utilized for studying other activated processes such as crystal growth in solutions.[95,96] However, such de-coupling might become possible for sufficiently long nanopores. Determining the critical pore length beyond which the docking and intra-pore diffusion processes become decoupled is an interesting question that will be addressed in future studies. One important—and convenient—consequence of such a decoupling will be that the passage rates will be proportional to the concentration difference between the two containers, with a proportionality constant known as permeability. The existence of coupling in our system makes this simple picture inaccurate, possibly resulting in a non-linear dependence of passage rate on concentration, a phenomenon previously observed, e.g., for H_2 flow through Pd membranes.[97] Understanding how mean passage times depend on concentration for short nanopores will therefore be an interesting area of future exploration.

Our calculations clearly demonstrate that there is a preferred sequence of crossing events, i.e., that the transport of the first chloride ion is likely to precede that of the first sodium. What is less certain, however, is whether any additional chlorides will traverse the pore in the interim, considering the wide separation of timescales between sodium and chloride transport. Mapping out the full sequence of crossing

events therefore requires determining passage times for all the relevant $F_{p,q} \rightarrow F_{p\pm1,q\pm1}$ transitions. The statistical behavior of the system can then be characterized by constructing a stochastic Markov model and utilizing computational methods, such as kinetic Monte Carlo. Such an exploration will be useful for systematically predicting solute transport rates and reversal potentials as a function of time for out-of-equilibrium processes such as filtration.

Our work demonstrates the power of advanced path-sampling techniques such as jFFS in exploring solute transport through nanoporous membranes and provides a scalable and efficient framework for studying the structure-selectivity relationship computationally. Such investigations, however, can benefit immensely from the development of more potent path-sampling techniques, more efficient order parameters, particularly for complex membrane and pore geometries, and more realistic force fields.

SUPPLEMENTAL INFORMATION

Supplemental Information can be found online at https://doi.org/10.1016/j.matt.2019.12.022.

ACKNOWLEDGMENTS

We thank P.G. Debenedetti, D. Limmer, and C. Ritt for useful discussions. A.H.-A. gratefully acknowledges the support of the National Science Foundation CAREER Award (grant no. CBET-1751971). These calculations were performed on the Yale Center for Research Computing. This work used the Extreme Science and Engineering Discovery Environment (XSEDE), which is supported by National Science Foundation grant no. ACI-1548562.[98] M.E. was supported by the NSF Nanosystems Engineering Research Center for Nanotechnology-Enabled Water Treatment (EEC1449500).

AUTHOR CONTRIBUTIONS

H.M., R.E., M.E., and A.H.-A. designed the research. H.M. and A.H.-A. performed the research, analyzed the data, and wrote the paper.

DECLARATION OF INTERESTS

The authors declare no competing interests.

Received: September 16, 2019
Revised: November 1, 2019
Accepted: December 18, 2019
Published: January 15, 2020

REFERENCES

1. Shannon, M.A., Bohn, P.W., Elimelech, M., Georgiadis, J.G., Mariñas, B.J., and Mayes, A.M. (2008). Science and technology for water purification in the coming decades. Nature *452*, 301–310.

2. Elimelech, M., and Phillip, W.A. (2011). The future of seawater desalination: energy, technology, and the environment. Science *333*, 712–717.

3. Koros, W.J., and Fleming, G. (1993). Membrane-based gas separation. J. Membr. Sci. *83*, 1–80.

4. Hutchings, G.S., and Altman, E.I. (2019). An atomically thin molecular aperture: two-dimensional gallium phosphate. Nanoscale Horiz. *4*, 667–673.

5. Cheng, W., Liu, C., Tong, T., Epsztein, R., Sun, M., Verduzco, R., Ma, J., and Elimelech, M. (2018). Selective removal of divalent cations by polyelectrolyte multilayer nanofiltration membrane: role of polyelectrolyte charge, ion size, and ionic strength. J. Membr. Sci. *559*, 98–106.

6. Marchetti, P., Jimenez Solomon, M.F., Szekely, G., and Livingston, A.G. (2014). Molecular separation with organic solvent nanofiltration: a critical review. Chem. Rev. *114*, 10735–10806.

7. Yang, S.Y., Ryu, I., Kim, H.Y., Kim, J.K., Jang, S.K., and Russell, T.P. (2006). Nanoporous membranes with ultrahigh selectivity and flux for the filtration of viruses. Adv. Mater. *18*, 709–712.

8. Gurtovenko, A.A., and Vattulainen, I. (2005). Pore formation coupled to ion transport through lipid membranes as induced by transmembrane ionic charge imbalance: atomistic molecular dynamics study. J. Am. Chem. Soc. *127*, 17570–17571.

9. Kumar, M., Grzelakowski, M., Zilles, J., Clark, M., and Meier, W. (2007). Highly permeable polymeric membranes based on the incorporation of the functional water channel

protein Aquaporin Z. Proc. Natl. Acad. Sci. U S A *104*, 20719–20724.

10. Holt, J.K., Park, H.G., Wang, Y., Stadermann, M., Artyukhin, A.B., Grigoropoulos, C.P., Noy, A., and Bakajin, O. (2006). Fast mass transport through sub-2-nanometer carbon nanotubes. Science *312*, 1034–1037.

11. Geise, G.M., Park, H.B., Sagle, A.C., Freeman, B.D., and McGrath, J.E. (2011). Water permeability and water/salt selectivity tradeoff in polymers for desalination. J. Membr. Sci. *369*, 130–138.

12. Nair, R., Wu, H., Jayaram, P., Grigorieva, I., and Geim, A. (2012). Unimpeded permeation of water through helium-leak–tight graphene-based membranes. Science *335*, 442–444.

13. Liu, K., Feng, J., Kis, A., and Radenovic, A. (2014). Atomically thin molybdenum disulfide nanopores with high sensitivity for DNA translocation. ACS Nano *8*, 2504–2511.

14. Werber, J.R., Osuji, C.O., and Elimelech, M. (2016). Materials for next-generation desalination and water purification membranes. Nat. Rev. Mater. *1*, 16018.

15. Sakiyama, Y., Mazur, A., Kapinos, L.E., and Lim, R.Y. (2016). Spatiotemporal dynamics of the nuclear pore complex transport barrier resolved by high-speed atomic force microscopy. Nat. Nanotechnol. *11*, 719.

16. Walker, M.I., Ubych, K., Saraswat, V., Chalklen, E.A., Braeuninger-Weimer, P., Caneva, S., Weatherup, R.S., Hofmann, S., and Keyser, U.F. (2017). Extrinsic cation selectivity of 2D membranes. ACS Nano *11*, 1340–1346.

17. Lively, R.P., and Sholl, D.S. (2017). From water to organics in membrane separations. Nat. Mater. *16*, 276–279.

18. Epsztein, R., Shaulsky, E., Dizge, N., Warsinger, D.M., and Elimelech, M. (2018a). Role of ionic charge density in Donnan exclusion of monovalent anions by nanofiltration. Environ. Sci. Technol. *52*, 4108–4116.

19. Epsztein, R., Cheng, W., Shaulsky, E., Dizge, N., and Elimelech, M. (2018b). Elucidating the mechanisms underlying the difference between chloride and nitrate rejection in nanofiltration. J. Membr. Sci. *548*, 694–701.

20. Boo, C., Wang, Y., Zucker, I., Choo, Y., Osuji, C.O., and Elimelech, M. (2018). High performance nanofiltration membrane for effective removal of perfluoroalkyl substances at high water recovery. Environ. Sci. Technol. *52*, 7279–7288.

21. der Bruggen, B.V., Koninckx, A., and Vandecasteele, C. (2004). Separation of monovalent and divalent ions from aqueous solution by electrodialysis and nanofiltration. Water Res. *38*, 1347–1353.

22. Deen, W.M. (1987). Hindered transport of large molecules in liquid-filled pores. AiChE J. *33*, 1409–1425.

23. Corry, B. (2008). Designing carbon nanotube membranes for efficient water desalination. J. Phys. Chem. B *112*, 1427–1434.

24. Song, C., and Corry, B. (2009). Intrinsic ion selectivity of narrow hydrophobic pores. J. Phys. Chem. B *113*, 7642–7649.

25. Richards, L.A., Schäfer, A.I., Richards, B.S., and Corry, B. (2012a). Quantifying barriers to monovalent anion transport in narrow non-polar pores. Phys. Chem. Chem. Phys. *14*, 11633–11638.

26. Richards, L.A., Schäfer, A.I., Richards, B.S., and Corry, B. (2012b). The importance of dehydration in determining ion transport in narrow pores. Small *8*, 1701–1709.

27. Sahu, S., and Zwolak, M. (2017). Ionic selectivity and filtration from fragmented dehydration in multilayer graphene nanopores. Nanoscale *9*, 11424–11428.

28. Epsztein, R., Shaulsky, E., Qin, M., and Elimelech, M. (2019). Activation behavior for ion permeation in ion-exchange membranes: role of ion dehydration in selective transport. J. Membr. Sci. *580*, 316–326.

29. Grosjean, B., Bocquet, M.-L., and Vuilleumier, R. (2019). Versatile electrification of two-dimensional nanomaterials in water. Nat. Commun. *10*, 1656.

30. Marbach, S., Dean, D.S., and Bocquet, L. (2018). Transport and dispersion across wiggling nanopores. Nat. Phys. *14*, 1108.

31. Cohen-Tanugi, D., and Grossman, J.C. (2012). Water desalination across nanoporous graphene. Nano Lett. *12*, 3602–3608.

32. Heiranian, M., Farimani, A.B., and Aluru, N.R. (2015). Water desalination with a single-layer MoS_2 nanopore. Nat. Commun. *6*, 8616.

33. Cohen-Tanugi, D., Lin, L.-C., and Grossman, J.C. (2016). Multilayer nanoporous graphene membranes for water desalination. Nano Lett. *16*, 1027–1033.

34. Chen, B., Jiang, H., Liu, X., and Hu, X. (2017). Molecular insight into water desalination across multilayer graphene oxide membranes. ACS Appl. Mater. Interfaces *9*, 22826–22836.

35. Dahanayaka, M., Liu, B., Hu, Z., Pei, Q.-X., Chen, Z., Law, A.W.-K., and Zhou, K. (2017). Graphene membranes with nanoslits for seawater desalination via forward osmosis. Phys. Chem. Chem. Phys. *19*, 30551–30561.

36. Konatham, D., Yu, J., Ho, T.A., and Striolo, A. (2013). Simulation insights for graphene-based water desalination membranes. Langmuir *29*, 11884–11897.

37. Sahu, S., Di Ventra, M., and Zwolak, M. (2017). Dehydration as a universal mechanism for ion selectivity in graphene and other atomically thin pores. Nano Lett. *17*, 4719–4724.

38. Alder, B.J., and Wainwright, T.E. (1959). Studies in molecular dynamics. I. General method. J. Chem. Phys. *31*, 459–466.

39. Torrie, G., and Valleau, J. (1977). Nonphysical sampling distributions in Monte Carlo free-energy estimation: umbrella sampling. J. Comp. Physiol. *23*, 187–199.

40. Haji-Akbari, A. (2018). Forward-flux sampling with jumpy order parameters. J. Chem. Phys. *149*, 072303.

41. Sint, K., Wang, B., and Král, P. (2008). Selective ion passage through functionalized graphene nanopores. J. Am. Chem. Soc. *130*, 16448–16449.

42. Tunuguntla, R.H., Henley, R.Y., Yao, Y.-C., Pham, T.A., Wanunu, M., and Noy, A. (2017). Enhanced water permeability and tunable ion selectivity in subnanometer carbon nanotube porins. Science *357*, 792–796.

43. Valeriani, C., Sanz, E., and Frenkel, D. (2005). Rate of homogeneous crystal nucleation in molten NaCl. J. Chem. Phys. *122*, 194501.

44. Li, T., Donadio, D., Ghiringhelli, L.M., and Galli, G. (2009). Surface-induced crystallization in supercooled tetrahedral liquids. Nat. Mater. *8*, 726–730.

45. Li, T., Donadio, D., Russo, G., and Galli, G. (2011). Homogeneous ice nucleation from supercooled water. Phys. Chem. Chem. Phys. *13*, 19807–19813.

46. Thapar, V., and Escobedo, F.A. (2014). Localized orientational order chaperones the nucleation of rotator phases in hard polyhedral particles. Phys. Rev. Lett. *112*, 048301.

47. Haji-Akbari, A., DeFever, R.S., Sarupria, S., and Debenedetti, P.G. (2014). Suppression of sub-surface freezing in free-standing thin films of a coarse-grained model of water. Phys. Chem. Chem. Phys. *16*, 25916–25927.

48. Haji-Akbari, A., and Debenedetti, P.G. (2015). Direct calculation of ice homogeneous nucleation rate for a molecular model of water. Proc. Natl. Acad. Sci. U S A *112*, 10582–10588.

49. Gianetti, M.M., Haji-Akbari, A., Longinotti, M.P., and Debenedetti, P.G. (2016). Computational investigation of structure, dynamics and nucleation kinetics of a family of modified Stillinger–Weber model fluids in bulk and free-standing thin films. Phys. Chem. Chem. Phys. *18*, 4102–4111.

50. Haji-Akbari, A., and Debenedetti, P.G. (2017). Computational investigation of surface freezing in a molecular model of water. Proc. Natl. Acad. Sci. U S A *114*, 3316–3321.

51. Jiang, H., Haji-Akbari, A., Debenedetti, P.G., and Panagiotopoulos, A.Z. (2018). Forward flux sampling calculation of homogeneous nucleation rates from aqueous NaCl solutions. J. Chem. Phys. *148*, 044505.

52. Sharma, S., and Debenedetti, P.G. (2012). Evaporation rate of water in hydrophobic confinement. Proc. Natl. Acad. Sci. U S A *109*, 4365–4370.

53. Altabet, Y.E., Haji-Akbari, A., and Debenedetti, P.G. (2017). Effect of material flexibility on the thermodynamics and kinetics of hydrophobically induced evaporation of water. Proc. Natl. Acad. Sci. U S A *114*, E2548–E2555.

54. Borrero, E.E., and Escobedo, F.A. (2006). Folding kinetics of a lattice protein via a forward flux sampling approach. J. Chem. Phys. *125*, 164904.

55. Suk, M.E., and Aluru, N.R. (2010). Water transport through ultrathin graphene. J. Phys. Chem. Lett. *1*, 1590–1594.

56. Wang, Y., He, Z., Gupta, K.M., Shi, Q., and Lu, R. (2017). Molecular dynamics study on water desalination through functionalized nanoporous graphene. Carbon *116*, 120–127.

57. Lee, J., Yang, Z., Zhou, W., Pennycook, S.J., Pantelides, S.T., and Chisholm, M.F. (2014).

Stabilization of graphene nanopore. Proc. Natl. Acad. Sci. U S A *111*, 7522–7526.

58. Price, D.J., and Brooks, C.L. (2004). A modified TIP3P water potential for simulation with Ewald summation. J. Chem. Phys. *121*, 10096–10103.

59. Müller-Plathe, F. (1996). Local structure and dynamics in solvent-swollen polymers. Macromolecules *29*, 4782–4791.

60. Joung, I.S., and Cheatham, T.E. (2008). Determination of alkali and halide monovalent ion parameters for use in explicitly solvated biomolecular simulations. J. Phys. Chem. B *112*, 9020–9041.

61. Beu, T.A. (2010). Molecular dynamics simulations of ion transport through carbon nanotubes. I. Influence of geometry, ion specificity, and many-body interactions. J. Chem. Phys. *132*, 164513.

62. Martínez, L., Andrade, R., Birgin, E.G., and Martínez, J.M. (2009). PACKMOL: a package for building initial configurations for molecular dynamics simulations. J. Comput. Chem. *30*, 2157–2164.

63. Plimpton, S. (1995). Fast parallel algorithms for short-range molecular dynamics. J. Comput. Phys. *117*, 1–19.

64. Bitzek, E., Koskinen, P., Gähler, F., Moseler, M., and Gumbsch, P. (2006). Structural relaxation made simple. Phys. Rev. Lett. *97*, 170201.

65. Swope, W.C., Andersen, H.C., Berens, P.H., and Wilson, K.R. (1982). A computer simulation method for the calculation of equilibrium constants for the formation of physical clusters of molecules: application to small water clusters. J. Chem. Phys. *76*, 637–649.

66. Nosé, S. (1984). A molecular dynamics method for simulations in the canonical ensemble. Mol. Phys. *52*, 255–268.

67. Hoover, W.G. (1985). Canonical dynamics: equilibrium phase-space distributions. Phys. Rev. A *31*, 1695–1697.

68. Ryckaert, J., Ciccotti, G., and Berendsen, H. (1977). Numerical integration of the cartesian equations of motion of a system with constraints: molecular dynamics of *n*-alkanes. J. Comput. Phys. *23*, 327–341.

69. Hockney, R.W., and Eastwood, J.W. (1989). Computer Simulation Using Particles (CRC Press).

70. Bostick, D., and Berkowitz, M.L. (2003). The implementation of slab geometry for membrane-channel molecular dynamics simulations. Biophys. J. *85*, 97–107.

71. Nguyen, T.D., Carrillo, J.-M.Y., Dobrynin, A.V., and Brown, W.M. (2012). A case study of truncated electrostatics for simulation of polyelectrolyte brushes on GPU accelerators. J. Chem. Theory Comput. *9*, 73–83.

72. Allen, R.J., Frenkel, D., and ten Wolde, P.R. (2006). Simulating rare events in equilibrium or nonequilibrium stochastic systems. J. Chem. Phys. *124*, 024102.

73. Gary-Bobo, C., and Solomon, A. (1971). Effect of geometrical and chemical constraints on water flux across artificial membranes. J. Gen. Physiol. *57*, 610–622.

74. Mehdizadeh, H., Dickson, J.M., and Eriksson, P.K. (1989). Temperature effects on the performance of thin-film composite, aromatic polyamide membranes. Ind. Eng. Chem. Chem. *28*, 814–824.

75. Richards, L.A., Richards, B.S., Corry, B., and Schäfer, A.I. (2013). Experimental energy barriers to anions transporting through nanofiltration membranes. Environ. Sci. Technol. *47*, 1968–1976.

76. Venable, R.M., Hatcher, E., Guvench, O., MacKerell, A.D., Jr., and Pastor, R.W. (2010). Comparing simulated and experimental translation and rotation constants: range of validity for viscosity scaling. J. Phys. Chem. B *114*, 12501–12507.

77. Kestin, J., Sokolov, M., and Wakeham, W. (1978). Viscosity of liquid water in the range -8 to 150. J. Phys. Chem. Ref. Data *7*, 941–948.

78. Chen, J.-Y., Nomura, H., and Pusch, W. (1983). Temperature dependence of membrane transport parameters in hyperfiltration. Desalination *46*, 437–446.

79. Sutera, S.P., and Skalak, R. (1993). The history of Poiseuille's law. Annu. Rev. Fluid Mech. *25*, 1–20.

80. Molinero, V., and Moore, E.B. (2009). Water modeled as an intermediate element between carbon and silicon. J. Phys. Chem. B *113*, 4008–4016.

81. Takaba, H., Onumata, Y., and Nakao, S.-I. (2007). Molecular simulation of pressure-driven fluid flow in nanoporous membranes. J. Chem. Phys. *127*, 054703.

82. Goldsmith, J., and Martens, C.C. (2009). Molecular dynamics simulation of salt rejection in model surface-modified nanopores. J. Phys. Chem. Lett. *1*, 528–535.

83. Wei, N., Peng, X., and Xu, Z. (2014). Understanding water permeation in graphene oxide membranes. ACS Appl. Mater. Interfaces *6*, 5877–5883.

84. Chen, B., Jiang, H., Liu, X., and Hu, X. (2017). Observation and analysis of water transport through graphene oxide interlamination. J. Phys. Chem. C *121*, 1321–1328.

85. Horner, A., Zocher, F., Preiner, J., Ollinger, N., Siligan, C., Akimov, S.A., and Pohl, P. (2015). The mobility of single-file water molecules is governed by the number of H-bonds they may form with channel-lining residues. Sci. Adv. *1*, e1400083.

86. Thapar, V., and Escobedo, F.A. (2015). Simultaneous estimation of free energies and rates using forward flux sampling and mean first passage times. J. Chem. Phys. *143*, 244113.

87. Rollings, R.C., Kuan, A.T., and Golovchenko, J.A. (2016). Ion selectivity of graphene nanopores. Nat. Commun. *7*, 11408.

88. Hodgkin, A.L., Huxley, A.F., and Katz, B. (1952). Measurement of current-voltage relations in the membrane of the giant axon of *Loligo*. J. Physiol. *116*, 424–448.

89. Krol, J., Wessling, M., and Strathmann, H. (1999). Concentration polarization with monopolar ion exchange membranes: current–voltage curves and water dissociation. J. Membr. Sci. *162*, 145–154.

90. Tedesco, M., Hamelers, H., and Biesheuvel, P. (2016). Nernst-Planck transport theory for (reverse) electrodialysis: I. Effect of co-ion transport through the membranes. J. Membr. Sci. *510*, 370–381.

91. Noskov, S.Y., Berneche, S., and Roux, B. (2004). Control of ion selectivity in potassium channels by electrostatic and dynamic properties of carbonyl ligands. Nature *431*, 830.

92. Wernersson, E., and Jungwirth, P. (2010). Effect of water polarizability on the properties of solutions of polyvalent ions: simulations of aqueous sodium sulfate with different force fields. J. Chem. Theory Comput. *6*, 3233–3240.

93. Kohagen, M., Mason, P.E., and Jungwirth, P. (2015). Accounting for electronic polarization effects in aqueous sodium chloride via molecular dynamics aided by neutron scattering. J. Phys. Chem. B *120*, 1454–1460.

94. Duan, Y., and Kollman, P.A. (1998). Pathways to a protein folding intermediate observed in a 1-microsecond simulation in aqueous solution. Science *282*, 740–744.

95. Joswiak, M.N., Doherty, M.F., and Peters, B. (2018a). Ion dissolution mechanism and kinetics at kink sites on NaCl surfaces. Proc. Natl. Acad. Sci. U S A *115*, 656–661.

96. Joswiak, M.N., Peters, B., and Doherty, M.F. (2018b). In silico crystal growth rate prediction for NaCl from aqueous solution. Cryst. Growth Des. *18*, 6302–6306.

97. Ward, T.L., and Dao, T. (1999). Model of hydrogen permeation behavior in palladium membranes. J. Membr. Sci. *153*, 211–231.

98. Towns, J., Cockerill, T., Dahan, M., Foster, I., Gaither, K., Grimshaw, A., Hazlewood, V., Lathrop, S., Lifka, D., Peterson, G.D., et al. (2014). XSEDE: accelerating scientific Discovery. Comput. Sci. Eng. *16*, 62–74.